



1 Geomagnetic influence on aircraft radiation 2 exposure during a solar energetic particle 3 event in October 2003

4 Christopher J. Mertens,¹ Brian T. Kress,² Michael Wiltberger,³ Steve R. Blattmig,¹
5 Tony S. Slaba,^{1,4} Stanley C. Solomon,³ and M. Engel⁵

6 Received 24 April 2009; revised 19 December 2009; accepted 20 December 2009; published XX Month 2010.

7 [1] We present initial results from the Nowcast of Atmospheric Ionizing Radiation for Aviation Safety
8 (NAIRAS) model during the Halloween 2003 superstorm. The objective of NAIRAS is to produce global,
9 real-time, data-driven predictions of ionizing radiation for archiving and assessing the biologically
10 harmful radiation exposure levels at commercial airline altitudes. We have conducted a case study of
11 radiation exposure during a high-energy solar energetic particle (SEP) event in October 2003. The
12 purpose of the case study is to quantify the important influences of the storm time and quiet time
13 magnetospheric magnetic field on high-latitude SEP atmospheric radiation exposure. The Halloween
14 2003 superstorm is an ideal event to study magnetospheric influences on atmospheric radiation
15 exposure since this event was accompanied by a major magnetic storm which was one of the largest of
16 solar cycle 23. We find that neglecting geomagnetic storm effects during SEP events can underestimate
17 the high-latitude radiation exposure from nearly 15% to over a factor of 2, depending on the flight
18 path relative to the magnetosphere open-closed boundary.

19 **Citation:** Mertens, C. J., B. T. Kress, M. Wiltberger, S. R. Blattmig, T. S. Slaba, S. C. Solomon, and M. Engel (2010),
20 Geomagnetic influence on aircraft radiation exposure during a solar energetic particle event in October 2003, *Space*
21 *Weather*, 8, XXXXXX, doi:10.1029/2009SW000487.

22 1. Introduction

23 [2] An important atmospheric state variable, driven by
24 space weather phenomena, is the ionizing radiation field.
25 The two sources of atmospheric ionizing radiation are
26 (1) the ever present, background galactic cosmic rays
27 (GCR), with origins outside the solar system, and (2) the
28 transient solar energetic particle (SEP) events, which are
29 associated with eruptions on the Sun's surface lasting for
30 several hours to days with widely varying intensity.
31 Quantifying the levels of atmospheric ionizing radiation
32 is of particular interest to the aviation industry since it is
33 the primary source of human exposure to high linear
34 energy transfer (LET) radiation. This radiation is effective
35 at directly breaking DNA strands in biological tissue, or

producing chemically active radicals in tissue that alter 36
the cell function, both of which can lead to cancer or other 37
adverse health effects. Consequently, there is increased 38
concern about potential health outcomes among passen- 39
gers and crew in the commercial and private aviation sector 40
[Wilson *et al.*, 2005b, 2003]. As a result, there is growing 41
need for a capability to predict the real-time radiation 42
levels at airline altitudes in order to (1) provide a contin- 43
uous assessment of ionizing radiation exposure for track- 44
ing aircrew exposure levels, (2) provide time-critical data 45
during SEP events for aviation radiation risk evaluation 46
and mitigation, and (3) provide an archived database of 47
radiation exposure for assessing the impact of ionizing 48
radiation on the global air transportation system as a whole, 49
especially in view of the current and future exponential 50
growth in the number of polar routes. The polar region 51
receives the largest quantity of radiation because the 52
shielding provided by Earth's magnetic field rapidly 53
approaches zero near the magnetic pole. 54

[3] Currently under development is the Nowcast of 55
Atmospheric Ionizing Radiation for Aviation Safety 56
(NAIRAS) model [Mertens *et al.*, 2008]. The goal of NAIRAS 57
is to provide a data-driven, global, real-time prediction of 58
ionizing radiation exposure from the surface to approxi- 59

¹NASA Langley Research Center, Hampton, Virginia, USA.

²Department of Physics and Astronomy, Dartmouth College, Hanover, New Hampshire, USA.

³High Altitude Observatory, National Center for Atmospheric Research, Boulder, Colorado, USA.

⁴Department of Mathematics and Statistics, Old Dominion University, Norfolk, Virginia, USA.

⁵Department of Physics, Hamline University, Saint Paul, Minnesota, USA.

60 mately 100 km. NAIRAS has adopted, as far as possible,
 61 the meteorological weather forecasting paradigm of com-
 62 bining physics-based forecast models with data assimi-
 63 lation techniques. The physics-based model we use to
 64 transport the ionizing radiation through the atmosphere
 65 and calculate the dosimetric quantities is the High charge
 66 (Z) and Energy Transport (HZETRN) code [Wilson *et al.*,
 67 1991]. While the quantity of observations relevant to radi-
 68 ation exposure predictions is currently too sparse to apply
 69 data assimilation techniques per se, nevertheless, we utilize
 70 as much real-time measurement data as possible to char-
 71 acterize the sources of ionizing radiation incident at the top
 72 of the atmosphere and the material properties of the at-
 73 mosphere necessary to understand the transport and
 74 transmutations of the sources of ionizing radiation through
 75 the atmosphere.

76 [4] There are a number of models currently in use for
 77 calculating GCR radiation exposure at aircraft altitudes.
 78 The CARI-6 model utilizes a database of transport calcu-
 79 lations generated by the deterministic LUN code for a
 80 wide variety of geographic locations, altitudes, and solar
 81 activity levels [O'Brien *et al.*, 2003, 1998]. The EPCARD
 82 model is based on a similar approach, but uses the Monte
 83 Carlo FLUKA code for the transport calculations [Schraube
 84 *et al.*, 1999]. PC-AIRE is a semiempirical model based on
 85 fits to measurement data [Lewis *et al.*, 2002]. Other aircraft
 86 radiation exposure models are described in the recent
 87 European Radiation Dosimetry Group report [Lindborg
 88 *et al.*, 2004]. Currently, the above models calculate SEP
 89 atmospheric radiation exposure poststorm on a case-by-
 90 case basis, although PC-AIRE incorporated low-Earth orbit
 91 measurements to develop a simple extrapolation to SEP
 92 events [Lewis *et al.*, 2002]. Recently, Copeland *et al.* [2008]
 93 calculated adult and conceptus aircraft exposure rates
 94 for 170 SEP events for years 1986–2008 using the Monte
 95 Carlo MCNPX transport code.

96 [5] The main differences that distinguish the NAIRAS
 97 model from the models discussed above are the following.
 98 The physics-based deterministic HZETRN transport cal-
 99 culations used in NAIRAS are continuously updated using
 100 real-time measurements of the space radiation environ-
 101 ment and of atmospheric density versus altitude. Further-
 102 more, both GCR and SEP atmospheric radiation exposure
 103 predictions are included in real time. And finally, dynam-
 104 ical geomagnetic effects are routinely included in the
 105 NAIRAS radiation exposure calculations.

106 [6] In this paper we conduct a case study and focus solely
 107 on SEP aircraft radiation exposure during the Halloween
 108 2003 superstorm. The specific time interval analyzed is
 109 from 29 October (2100 UT) through 31 October (2400 UT).
 110 The primary objective of this case study is to diagnose the
 111 influence of geomagnetic storm effects on SEP atmospheric
 112 radiation exposure. The interest in understanding aviation
 113 ionizing radiation, and SEP exposure in particular, is
 114 because the International Commission on Radiological
 115 Protection (ICRP), the Environmental Protection Agency
 116 (EPA), and the Federal Aviation Administration (FAA)
 117 consider crews of commercial aircraft as radiation workers

[McMeekin, 1990; ICRP, 1991]. However, aircrew are currently 118
 not monitored for radiation exposure, nor are passengers 119
 aware of any potential radiation risks. Reproductive dis- 120
 order, including prenatal injury, are a particular concern 121
 [Lauria *et al.*, 2006; Waters *et al.*, 2000; Aspholm *et al.*, 1999]. 122

[7] The importance of our case study is that we find 123
 geomagnetic storm effects to have a profound effect on 124
 SEP atmospheric radiation exposure. The Halloween 125
 2003 superstorm is an ideal event to study geomagnetic 126
 effects since this event contained a major magnetic storm 127
 which was one of the largest of solar cycle 23. The geo- 128
 magnetic storm effects are the consequence of solar wind- 129
 magnetosphere interactions that weaken the effective 130
 shielding of incident low-energy SEP ions by the Earth's 131
 magnetic field [Kress *et al.*, 2009]. The effect of a weakened 132
 magnetic field, in response to a geomagnetic storm, is a 133
 significant increase in SEP atmospheric ionizing radiation. 134
 This result underscores the need for continued space 135
 environment measurements and accurate models of solar 136
 wind-magnetosphere interactions. 137

[8] The outline of the rest of the paper is as follows. In 138
 section 2 we describe the measurement data and space 139
 environment models used to characterize the incident 140
 SEP particle flux at the top of the atmosphere, and the 141
 meteorological data and models used to characterize 142
 atmospheric density. Section 3 describes the transport of 143
 the incident SEP ion flux through the atmosphere and the 144
 calculation of radiation exposure. The high-energy SEP 145
 event during the Halloween 2003 superstorm is analyzed in 146
 section 4. A summary and conclusions are presented in 147
 section 5. 148

2. Data Input and Space Environment Models 149

[9] NAIRAS model predictions of atmospheric SEP 150
 radiation exposure are driven by measurements from the 151
 atmosphere and from space. Real-time satellite ion flux 152
 measurements are used to derive the SEP proton and alpha 153
 spectral fluence rates incident at the top of the atmosphere. 154
 The geomagnetic field (internal field plus magnetospheric 155
 contributions) filters the incident SEP spectral fluence rates 156
 by deflecting the lower-energy particles back out to space. 157
 This spectral filtering effect is quantified by a canonical 158
 variable called the geomagnetic cutoff rigidity. Satellite 159
 measurements of solar wind dynamical pressure and the 160
 interplanetary magnetic field (IMF) are used to characterize 161
 the magnetospheric contributions to the cutoff rigidity. 162
 Global meteorological measurements combined with data 163
 assimilation and forecast models are used to predict atmo- 164
 spheric depth as a function of altitude. In sections 2.1–2.3, 165
 we describe the data input and space environment models 166
 used to derive (1) the incident SEP spectral fluence rates, 167
 (2) the geomagnetic cutoff rigidity, and (3) atmospheric 168
 depth as a function of altitude. 169

2.1. SEP Spectral Fluence Rates 170

[10] The current understanding of SEP processes is that 171
 the energy spectrum is a result of injected particle seed 172

173 populations that are stochastically accelerated in a tur-
 174 bulent magnetic field associated with a CME-driven
 175 interplanetary shock [Tylka and Lee, 2006]. An analytical
 176 expression that represents the differential energy spec-
 177 trum for this shock acceleration mechanism was given
 178 by Ellison and Ramaty [1985], where the spectrum has
 179 the form

$$\frac{d^2J}{dEd\Omega} = C_a E^{-\gamma_a} \exp(-E/E_0). \quad (1)$$

180 The differential energy spectrum on the left-hand side
 181 of (1) has units of $\text{cm}^{-2} \text{sr}^{-1} \text{h}^{-1} (\text{MeV/n})^{-1}$, and the
 182 energy (E) has units of MeV n^{-1} (i.e., MeV per nucleon).
 183 The constant C_a is related to the injected seed population
 184 far upstream of the shock. The power law energy depen-
 185 dence of the spectrum is due to shock acceleration of the
 186 seed population by random first-order Fermi acceleration
 187 (scattering) events in a turbulent magnetic field, with the
 188 power index (γ_a) related to the shock compression ratio.
 189 The exponential turnover in (1) represents high-energy
 190 limits to the acceleration mechanism, such as escape from
 191 the shock region. Using the above analytical form, the
 192 three parameters (C_a , γ_a , and E_0) can be determined by
 193 fitting (1) to ion flux measurements.

194 [11] Recently, Mewaldt et al. [2005] found that the Ellison-
 195 Ramaty spectral form failed to fit NOAA/GOES ion flux
 196 measurements at the highest-energy channels during the
 197 Halloween 2003 SEP events. To circumvent this deficiency,
 198 Mewaldt et al. proposed using a double power law spec-
 199 trum. The low-energy spectrum is assumed to follow
 200 the Ellison-Ramaty form. The high-energy spectrum is
 201 assumed to have a power law energy dependence with
 202 a different power index, such that

$$\frac{d^2J}{dEd\Omega} = C_b E^{-\gamma_b}. \quad (2)$$

203 The power law expressions in (1) and (2) can be merged into
 204 one continuous spectrum by requiring that the differential
 205 energy spectra in (1) and (2) and their first derivatives are
 206 continuous at the merge energy. The result is given by the
 207 expression below:

$$\frac{d^2J}{dEd\Omega} = C E^{-\gamma_a} \exp(-E/E_0), E \leq (\gamma_b - \gamma_a)E_0 \quad (3)$$

$$= C E^{-\gamma_b} \left\{ [(\gamma_b - \gamma_a)E_0]^{(\gamma_b - \gamma_a)} \exp(\gamma_b - \gamma_a) \right\}, \\ E > (\gamma_b - \gamma_a)E_0. \quad (4)$$

208 Physically, the double power law spectrum in (3) and (4)
 209 represents SEP sources from two different injected seed
 210 populations. For example, the low-energy spectrum, with
 211 γ_a power index and the e-folding energy E_0 , is likely asso-
 212 ciated with solar corona (solar wind) seed populations
 213 while the high-energy spectrum, with γ_b power index, is

likely associated with flare suprathermal seed populations 214
 [Tylka et al., 2005]. 215

[12] The NAIRAS model initially assumes the double 216
 power law form in (3) and (4) for the SEP fluence spectrum 217
 and derives the fit parameters (C , γ_a , γ_b , and E_0) by a 218
 nonlinear least squares fit to differential-directional ion 219
 flux measurements. The spectral fitting algorithm uses a 220
 Marquardt-Levenberg iteration technique [Brandt, 1999]. If 221
 the double power law spectrum fails to converge to the 222
 measurement data, the fitting procedure is restarted and 223
 the Ellison-Ramaty spectral form is assumed. 224

[13] NAIRAS utilizes available real-time measurements 225
 of proton and alpha differential-directional particle flux 226
 ($\text{cm}^{-2} \text{sr}^{-1} \text{s}^{-1} (\text{MeV/n})^{-1}$) for the SEP spectral fitting 227
 described above. SEP spectral fluence rates ($\text{cm}^{-2} \text{h}^{-1}$ 228
 ($\text{MeV/n})^{-1}$) incident on Earth's atmosphere are obtained by 229
 time averaging the particle flux measurements in 1 h time 230
 bins and projecting the incident flux onto the vertical 231
 direction assuming an isotropic angular distribution for 232
 the solar ions. Low-energy proton data are obtained from 233
 the Electron, Proton, and Alpha Monitor (EPAM) instru- 234
 ment onboard the NASA Advanced Composition Explorer 235
 (ACE) satellite [Gold et al., 1998]. EPAM is composed of five 236
 telescopes and we use the LEMS120 (Low-Energy Mag- 237
 netic Spectrometer) detector, which measures ions at 238
 120 degrees from the spacecraft axis. LEMS120 is the 239
 EPAM low-energy ion data available in real time, for 240
 reasons described by Haggerty et al. [2006]. The other proton 241
 channels used in the SEP spectral fitting algorithm are 242
 obtained from NOAA's Geostationary Operational Envi- 243
 ronmental Satellite (GOES) Space Environment Monitor 244
 (SEM) measurements. The Energetic Particle Sensor (EPS) 245
 and the High Energy Proton and Alpha Detector (HEPAD) 246
 sensors on GOES/SEM measure differential-directional 247
 proton flux [Onsager et al., 1996]. We also generate addi- 248
 tional differential-directional proton flux measurement 249
 channels by taking differences between the EPS integral 250
 proton flux channels. The channels used to derive SEP 251
 alpha spectral fluence rates are also obtained from EPS 252
 measurements. We use 5 min averaged ACE and GOES 253
 data to derive the incident SEP spectral fluence rates. 254

[14] Figure 1 shows the time variation of a representative 255
 set of proton flux measurements used to derive incident 256
 SEP spectral fluence rates for the Halloween 2003 storm 257
 period. The two plots show the GOES 11 EPS and HEPAD 258
 proton flux spectra and the integral proton flux mea- 259
 surements. By definition, a SEP event occurs when the 260
 >10 MeV integral proton flux exceeds 10 proton flux units 261
 ($\text{pfu} \equiv \text{cm}^{-2} \text{sr}^{-1} \text{s}^{-1}$) in three consecutive 5 min periods 262
 [NOAA, 2009]. The SEP event threshold is denoted by the 263
 horizontal line in the integral proton flux plot (Figure 1, 264
 bottom). There are a total of five SEP events during the 265
 Halloween 2003 storm period, which are denoted by the 266
 vertical lines in both plots in Figure 1. These events were 267
 associated with many simultaneous, complex phenomena 268
 such as solar flares, coronal mass ejections (CME), inter- 269
 planetary shocks, and solar cosmic ray ground level events 270
 (GLE) [see Gopalswamy et al., 2005]. Different line styles 271

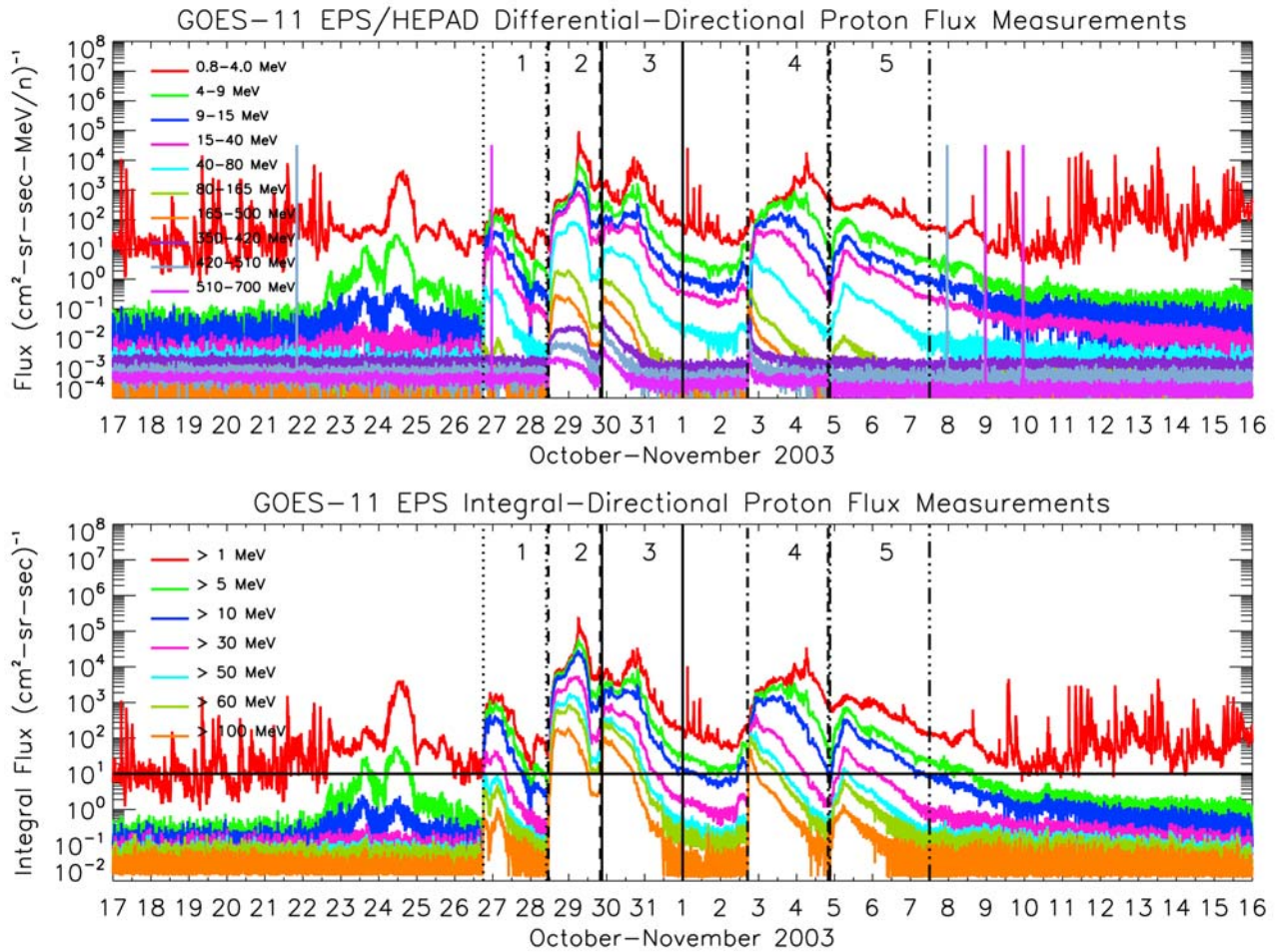


Figure 1. GOES 11 proton flux measurements: (top) the EPS/HEPAD differential-directional flux and (bottom) the EPS integral-directional flux. The color lines represent different GOES 11 proton channels, and the energy ranges of the channels are specified in the legend. The different vertical line styles bound the five SEP events, which are also numbered in both plots. See text for details.

272 are used to bound each of the five events, and the event
 273 number is shown between the vertical lines. Note that
 274 the onset of event 3 does not follow the conventional SEP
 275 threshold definition. It is clear from the integral proton
 276 flux that two events overlap: event 3 arrives before event
 277 2 decreases below the SEP threshold level. However, there
 278 is an important distinguishing feature between the two
 279 events. That is, the beginning of our definition of event 3
 280 is accompanied by a sudden increase in high-energy
 281 protons associated with the arriving SEP event, as noted
 282 by the sudden increase in the 510–700 MeV differential-
 283 directional proton flux measurements in Figure 1. Parti-
 284 tioning the simultaneous SEP events 2 and 3 into separate
 285 events is useful for our study, since the high-energy por-
 286 tion of the differential-directional proton flux distribution
 287 penetrates deeper in the atmosphere.

288 [15] We will analyze atmospheric ionizing radiation
 289 exposure during SEP event 3 (29 October (2100 UT) to

31 October (2400 UT)) since the associated interaction
 between the arriving CME-driven interplanetary shock
 and Earth's magnetosphere caused the largest geomag-
 netic effects during the Halloween 2003 storm period,
 which is the focus of our case study. In order to isolate the
 geomagnetic effects, we derived the event-averaged SEP
 spectral fluence rates shown in Figure 2. The horizontal lines
 in Figure 2 are the event-averaged differential-directional
 ion flux measurements. The width of the horizontal lines
 correspond to the energy width of the measurement
 channels. The black lines are the proton and alpha spectral
 fluence rates derived using the double power law spectrum
 and fitting technique describe above. The shaded regions
 show the range of 1 h averaged ion flux measurements in
 the time interval of event 3. The peach colored region
 corresponds to the range of proton flux measurements
 and the blue colored region corresponds to the alpha flux
 measurements. The event-averaged fit parameters derived

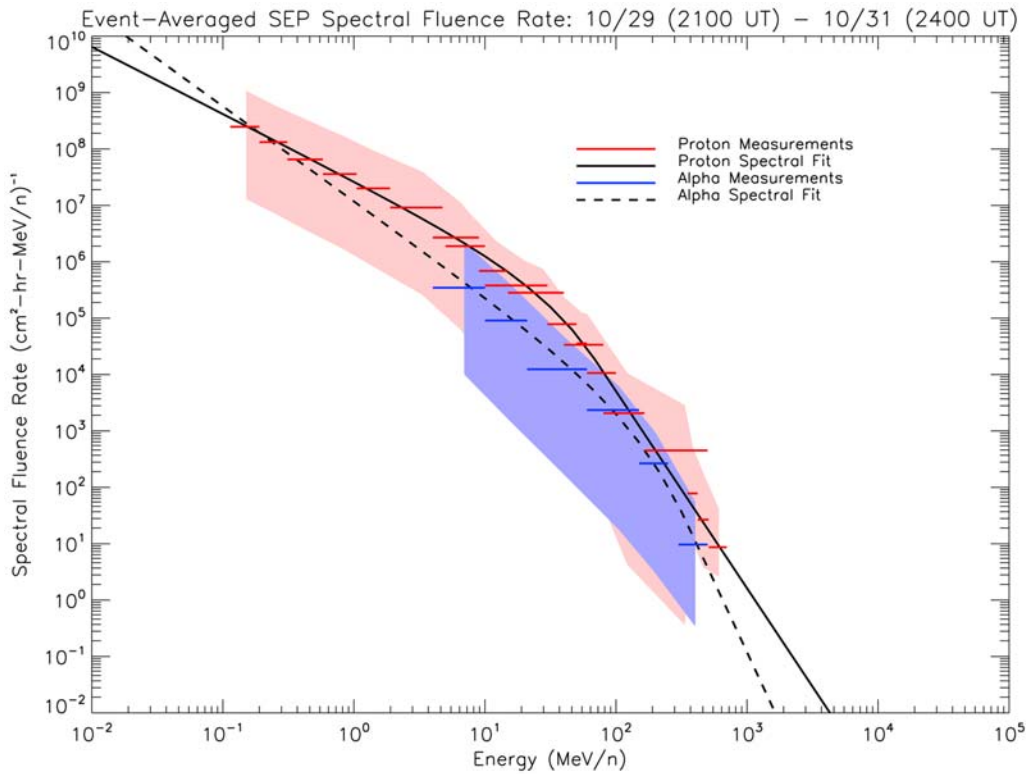


Figure 2. Event-averaged SEP spectral fluence rates for event 3 (29 October 2003 (2100 UT) to 31 October 2003 (2400 UT)). The shaded regions show the range of 1 h averaged ion flux measurements in the time interval of event 3. The peach shaded region corresponds to proton flux measurements. The blue shaded region corresponds to the alpha flux measurements.

308 for SEP event 3 are given in Table 1. Thus, equations (3)
 309 and (4) and the parameters in Table 1 characterize the
 310 incident SEP spectral fluence rates used in the analysis
 311 of atmospheric exposure in this paper. One can readily
 312 reproduce our incident SEP spectral fluence rate and
 313 compare with our computed exposure rates presented in
 314 section 4.

315 2.2. Geomagnetic Cutoff Rigidities

316 [16] The geomagnetic field provides a form of momen-
 317 tum shielding by deflecting lower-energy charged particles
 318 back out to space. The minimum momentum per unit
 319 charge that a vertically incident particle can have and still
 320 reach a given altitude above the Earth is called the vertical
 321 geomagnetic cutoff rigidity. The cutoff rigidity is a canon-
 322 ical variable for specifying the minimum access energy of
 323 incident charged particles (SEP particles in this study) for
 324 transport through the atmosphere. Once the cutoff rigidity
 325 is known, the minimum access energy is determined for
 326 each incident particle of charge Z and mass number A
 327 through the relativistic energy equation, such that

$$E = \left[\sqrt{R^2 (Z/A \cdot \text{amu} \cdot c^2)^2 + 1} - 1 \right] \cdot \text{amu} \cdot c^2, \quad (5)$$

where E is kinetic energy per nucleon (MeV n^{-1}), R is
 vertical geomagnetic cutoff rigidity (MV), c is the speed
 of light in vacuum, and $\text{amu} = 931.5 \text{ MeV } c^{-2}$ (atomic mass
 unit). 328 329 330 331

[17] The cutoff rigidity is determined by numerical solu-
 tion of charged particle trajectories in the geomagnetic field
 [Smart and Shea, 2005, 1994]. The NAIRAS cutoff rigidities
 are calculated from code developed by the Center for
 Integrated Space Weather Modeling (CISM) at Dartmouth
 College. The CISM, Dartmouth geomagnetic cutoff model
 can be run using several different empirical and physics-
 based models [Kress *et al.*, 2004]. In particular, the specifi-
 cation of the geomagnetic field due to Earth's internal field
 source is provided by the International Geomagnetic Ref-
 erence Field (IGRF) model [Langlais and Manda, 2000]. The 332 333 334 335 336 337 338 339 340 341 342

Table 1. Event-Averaged Fit Parameters^a

Particle	C	γ_a	γ_b	E_0
Proton	8.565×10^6	1.191	3.493	30.78
Alpha	3.782×10^6	1.682	4.992	105.3

^aEvent is from 29 October 2003 (2100 UT) to 31 October 2003
 (2400 UT). t1.1 t1.2 t1.3 t1.4 t1.5 t1.6

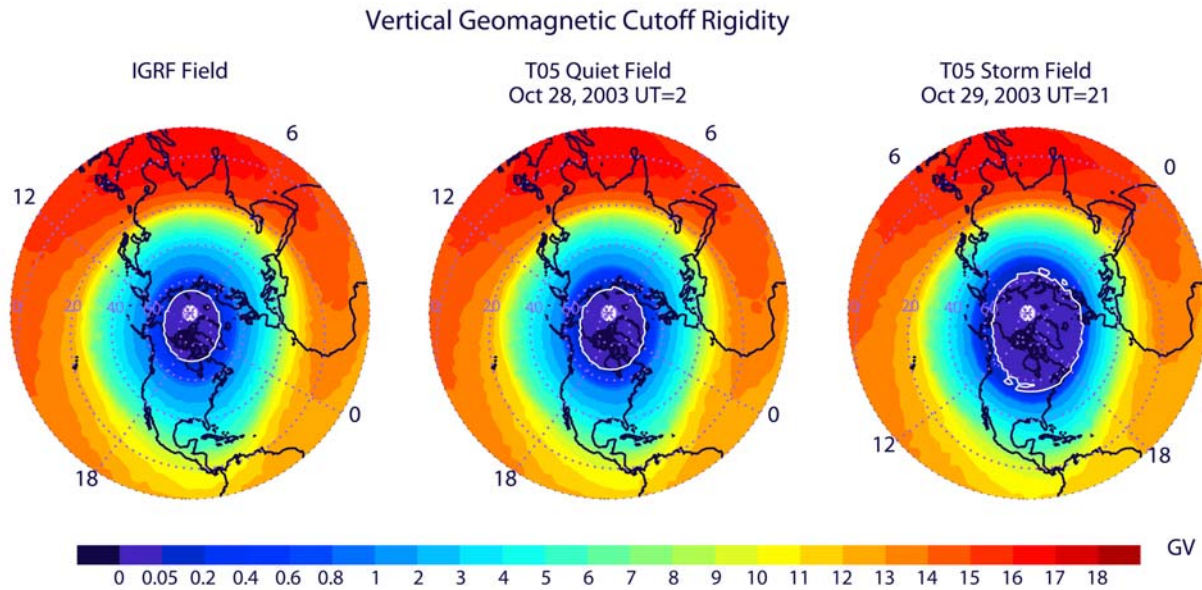


Figure 3. Simulated vertical geomagnetic cutoff rigidity shown over the Northern Hemisphere in October 2003. The cutoff rigidities were calculated using (left) the IGRF model, (middle) the T05 model during a geomagnetically quiet period, and (right) the T05 model during the largest geomagnetically disturbed period of SEP event 3. Also shown are the magnetic latitude circles and the meridians at 0000, 0600, 1200, and 1800 magnetic local time.

343 IGRF 2000 epoch is used in this study. The magnetospheric
 344 current systems are also important contributors to Earth's
 345 total geomagnetic field. The real-time dynamical response
 346 of the magnetospheric magnetic field to solar wind condi-
 347 tions and IMF can be provided by the semiempirical T05
 348 model [Tsyganenko and Sitnov, 2005], or by the Lyon-Feder-
 349 Mobarry (LFM) global MHD simulation code [Lyon et al.,
 350 2004]. Currently, the T05 model provides more accurate
 351 cutoff rigidities than the LFM MHD model, as deter-
 352 mined by comparisons with satellite observations during
 353 a Halloween 2003 geomagnetic storm [Kress et al., 2009].
 354 Thus, for the present work, the simulated real-time geo-
 355 magnetic cutoff rigidities are calculated using the T05
 356 model, and using the IGRF model for comparison.

357 [18] Figure 3 shows the vertical cutoff rigidity over the
 358 Northern Hemisphere for three different models of the
 359 geomagnetic field. Figure 3 (left) is cutoff rigidity computed
 360 using the IGRF field. Since total flight path exposures at
 361 aviation altitudes do not change significantly ($< \sim 1\%$) for
 362 cutoffs less than 0.05 GV, we set the cutoffs to zero at geo-
 363 graphic locations poleward of the 0.05 GV contour (see the
 364 bold white 0.05 GV color contour in Figure 3). Figure 3
 365 (middle) shows the cutoff rigidities computed using
 366 the T05 field under geomagnetically quiet conditions,
 367 28 October (0200 UT), prior to the onset of the Halloween
 368 2003 SEP event 3. One can see that even during magnet-
 369 ically quiet conditions, the cutoff rigidities predicted from
 370 the T05 field are lower than predicted from the IGRF
 371 field, and the polar cap region (i.e., inside the bold white

0.05 GV contour in Figure 3) is expanded to lower latitudes. 372
 A weaker field predicted by the T05 model, compared to 373
 IGRF, is due in part to the diamagnetic effect of the mag- 374
 netospheric ring current included in the T05 model. Lower 375
 cutoff rigidities correspond to less momentum shielding 376
 and higher radiation exposure levels. Figure 3 (right) shows 377
 the cutoff rigidities during peak geomagnetic storm condi- 378
 tions, 29 October (2100 UT), during SEP event 3. The 379
 cutoffs are lower at all latitudes compared to the two pre- 380
 vious simulations, and the polar cap region has expanded 381
 to much lower latitudes than during the magnetically quiet 382
 period. These geomagnetic effects are discussed in more 383
 detail in section 4. 384

2.3. Atmospheric Depth Altitude 385

[19] The atmosphere itself provides shielding from 386
 incident charged particles. The shielding of the atmosphere 387
 at a given altitude depends on the overhead mass. Subdaily 388
 global atmospheric depth is determined from pressure 389
 versus geopotential height and pressure versus temperature 390
 data derived from the National Center for Environmental 391
 Prediction (NCEP)/National Center for Atmospheric 392
 Research (NCAR) Reanalysis 1 project [Kalnay et al., 1996]. 393
 The NCAR/NCEP Reanalysis 1 project uses a state-of- 394
 the-art analysis/forecast system to perform data assimila- 395
 tion using past data from 1948 to the present. The data 396
 products are available 4X daily at 0000, 0600, 1200, and 397
 1800 UT. The spatial coverage is 17 pressure levels in the 398
 vertical from approximately the surface (1000 hPa) to the 399

NCAR/NCEP Reanalysis 1: Pressure at 11 km

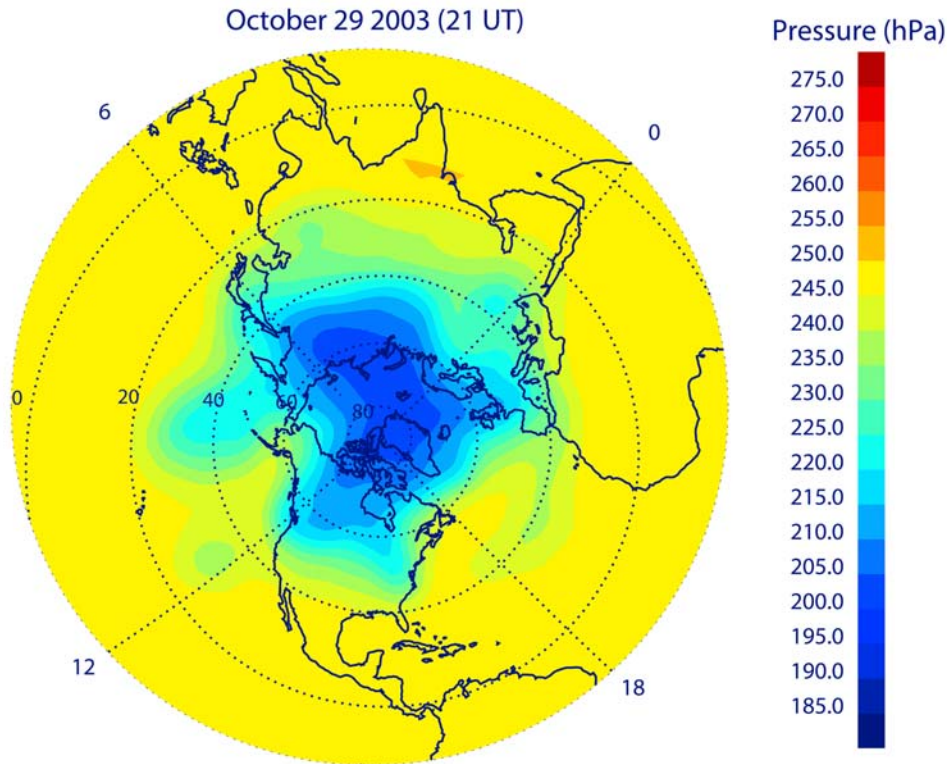


Figure 4. NCAR/NCEP Reanalysis 1 pressure levels at 11 km corresponding to the date/time of the largest geomagnetically disturbed period of SEP event 3 (29 October 2003, 2100 UT). Also shown are the magnetic latitude circles and the meridians at 0000, 0600, 1200, and 1800 magnetic local time.

400 middle stratosphere (10 hPa), while the horizontal grid is
401 2.5×2.5 degrees covering the entire globe.

402 [20] NCAR/NCEP pressure versus geopotential height
403 data is extended in altitude above 10 hPa using the Naval
404 Research Laboratory Mass Spectrometer and Incoherent
405 Scatter (NRLMSIS) model atmosphere [Picone *et al.*, 2002].
406 NCAR/NCEP and NRLMSIS temperatures are smoothly
407 merged at 10 hPa at each horizontal grid point. NRLMSIS
408 temperatures are produced at 2 km vertical spacing from
409 the altitude of the NCEP/NCAR 10 hPa pressure surface to
410 approximately 100 km. The pressure at these extended
411 altitudes can be determined from the barometric law using
412 the NRLMSIS temperature profile and the known NCAR/
413 NCEP 10 hPa pressure level, which assumes the atmo-
414 sphere is in hydrostatic equilibrium and obeys the ideal gas
415 law. Finally, the altitudes and temperatures are linearly
416 interpolated in log pressure to a fixed pressure grid from
417 1000 hPa to 0.001 hPa, with six pressure levels per decade.
418 The result from this step is pressure versus altitude at
419 each horizontal grid point from the surface to approxi-
420 mately 100 km.

421 [21] Atmospheric depth (g cm^{-2}) at each altitude level
422 and horizontal grid point is computed by vertically inte-

grating the mass density from a given altitude to the top of 423
the atmosphere. The mass density is determined by the 424
ideal gas law using the pressure and temperature at each 425
altitude level. The result from this step produces a 3-D 426
gridded field of atmospheric depth. Atmospheric depth at 427
any specified aircraft altitude is determined by linear 428
interpolation along the vertical grid axis in log atmo- 429
spheric depth. Figure 4 shows the atmospheric pressure 430
over the Northern Hemisphere at 11 km on 29 October 431
2003 (2100 UT). This is the atmospheric data used in the 432
exposure rate calculations in section 4. 433

3. SEP Transport and Dosimetry

434

[22] In section 2, we described the incident SEP spectral 435
fluence rates, cutoff rigidity, and atmospheric depth as a 436
function of altitude. In this section, we describe the 437
transport of the incident SEP ions through the atmosphere 438
and the subsequent absorbed dose in tissue from the 439
ionizing radiation field. 440

[23] SEP atmospheric transport is described by a coupled 441
system of linear Boltzmann transport equations, which are 442
derived on the basis of conservation principles [Wilson *et* 443

444 *al.*, 1991]. The transport equation for the spectral fluence
445 rate $\phi_j(\mathbf{x}, \Omega, E)$ for particle type j is given by

$$\Omega \cdot \nabla \Phi_j(\mathbf{x}, \Omega, E) = \sum_k \int \sigma_{jk}(\Omega, \Omega', E, E') \Phi(\mathbf{x}, \Omega', E') d\Omega' dE' - \sigma_j(E) \Phi(\mathbf{x}, \Omega, E), \quad (6)$$

446 where $\sigma_j(E)$ and $\sigma_{jk}(\Omega, \Omega', E, E')$ are the target medium
447 macroscopic cross sections. The $\sigma_{jk}(\Omega, \Omega', E, E')$ are double-
448 differential particle production cross sections that repre-
449 sent all processes by which type k particles moving in
450 direction Ω' with energy E' produce a particle of type j
451 moving in direction Ω with energy E , including radio-
452 active decay processes. The total cross section $\sigma_j(E)$ of the
453 target medium for each incident particle type j is

$$\sigma_j(E) = \sigma_{j,at}(E) + \sigma_{j,el}(E) + \sigma_{j,r}(E), \quad (7)$$

454 where the first term refers to collisions with atomic
455 electrons, the second term refers to elastic ion-nucleus
456 scattering, or elastic neutron-neutron scattering, and the
457 third term contains all relevant nuclear reactions. The
458 corresponding differential cross sections are similarly
459 ordered.

460 [24] The coupled SEP transport equations in (6) are
461 solved in the NAIRAS model using NASA Langley
462 Research Center's deterministic HZETRN code. HZETRN
463 is used in a wide variety of radiation transport applications,
464 e.g., the calculation of dosimetric quantities for assessing
465 astronaut risk to space radiations on the International
466 Space Station (ISS) and the Space Transportation System
467 (STS) Shuttle, and for design and validation of the Crew
468 Exploration Vehicle (CEV) under the Constellation pro-
469 gram, including realistic spacecraft and human geometry
470 [Slaba *et al.*, 2009; Badavi *et al.*, 2007a, 2005; Wilson *et al.*,
471 2006]. Extensive summaries of HZETRN laboratory and
472 space flight verification and validation are found in recent
473 reports by Badavi *et al.* [2007a], Nealy *et al.* [2007], and Wilson
474 *et al.* [2005a, 2005c].

475 [25] For SEP proton and alpha particles incident at the
476 top of the atmosphere, solutions to six coupled transport
477 equations are obtained: one for neutrons and five for light
478 ions (protons, deuterons, tritons, helium-3, and helium-4).
479 A recent update to HZETRN includes a directionally
480 coupled forward-backward low-energy neutron transport
481 algorithm, which is important for atmospheric radiation
482 transport (T. C. Slaba *et al.*, Coupled neutron transport for
483 HZETRN, submitted to *Advances in Space Research*, 2008).

484 [26] The energy deposited in a target medium by the
485 radiation field of particle j is the dose, which is given by

$$D_j(\mathbf{x}) = K \int_{\Omega} \int_0^{\infty} S_j(E) \Phi_j(\mathbf{x}, \Omega, E) d\Omega dE. \quad (8)$$

486 In the above equation, $S_j(E)$ is the target stopping power for
487 particle j ($\text{MeV g}^{-1} \text{cm}^{-2}$) and K is a unit conversion factor
488 (1.602×10^{-10}) to convert dose to units of Gray ($1 \text{ Gy} = \text{J kg}^{-1}$).
489 Radiation health risk and the probability of biological

490 damage depend not only on the absorbed dose, but also
491 on the particle type and energy of the radiation causing
492 the dose. This is taken into account by weighting the
493 absorbed dose by a factor related to the quality of the
494 radiation. The weighted absorbed dose has been given
495 the name dose equivalent by ICRP [1991]. The unit of
496 dose equivalent is the Sievert (Sv). Dose equivalent in
497 tissue T from particle j ($H_{j,T}(\mathbf{x})$) is defined in terms of the
498 tissue LET-dependent quality factor Q , such that

$$H_{j,T}(\mathbf{x}) = \int_L Q(L) D_j(\mathbf{x}, L) dL, \quad (9)$$

499 where L is LET, which can be approximated by the
500 stopping power in units of $\text{keV } \mu\text{m}^{-1}$; $D_j(\mathbf{x}, L)$ is the
501 spectral dose distribution from particle j in terms of LET,
502 and $Q(L)$ is the tissue LET-dependent quality factor.

503 [27] The relationship between the probability of biolog-
504 ical damage and dose equivalent is found to also depend
505 on the organ or tissue irradiated. A further dosimetric
506 quantity, called the effective dose, is defined to include the
507 relative contributions of each organ or tissue to the total
508 biological detriment caused by radiation exposure. The
509 effective dose ($E(\mathbf{x})$) is the sum of weighted dose equiva-
510 lents in all the organs and tissues in the human body, such
511 that

$$E(\mathbf{x}) = \sum_T \sum_j w_T H_{j,T}(\mathbf{x}). \quad (10)$$

512 The organ/tissue weighting factors are given in the ICRP
513 60 report [ICRP, 1991]. A computationally efficient approach
514 is to calculate the effective dose rates directly from the par-
515 ticle spectral fluence rates using precomputed fluence-to-
516 effective dose conversion coefficients. In this paper we use
517 neutron and proton conversion coefficients tabulated by
518 Ferrari *et al.* [1997a, 1997b]. The effective dose contributions
519 from the other ions are obtained by scaling the proton
520 fluence-to-effective dose conversion coefficients by Z_j^2/A_j ,
521 according to stopping power dependence on charge and
522 mass. All recommended ICRP radiation exposure limits
523 are defined in terms of effective dose.

524 [28] The assumptions and simplifications to our transport
525 calculations and dosimetric predictions presented in
526 section 4 are briefly described here. We assume that the
527 incident SEP ion are isotropically distributed in angle, and
528 we project the ions along the vertical direction to obtain
529 the incident SEP spectral fluence rates in the calculation
530 of effective dose in (8)–(10). Moreover, we assume the
531 minimum access energies for the incident ions are deter-
532 mined by the vertical cutoff rigidities described in
533 section 2.2. Finally, we ignore the influence of the air-
534 craft structure on the radiation field. None of the existing
535 atmospheric radiation models include aircraft structure
536 effects operationally; however, some cases studies have
537 been done. The aircraft may reduce the free atmosphere
538 radiation exposure by perhaps $\sim 10\%$ for GCR exposure
539 [Battistoni *et al.*, 2005; Copeland *et al.*, 2008] and less than
540 1% for SEP events [Copeland *et al.*, 2008]. Future updates to

540 NAIRAS will include transport through the aircraft fuse-
 541 lage, utilizing the methodologies developed for astronaut
 542 radiation risk assessment [Badavi et al., 2007b; Slaba et al.,
 543 2009], and quantify the directional effects on the cutoff
 544 rigidities and their subsequent influence on the radiation
 545 exposure.

546 4. Analysis of Halloween 2003 Event

547 [29] In this section we present our predictions of SEP
 548 effective dose rates and accumulated effective dose along
 549 representative high-latitude commercial routes during
 550 the Halloween 2003 SEP event 3 (29 October (2100 UT) to
 551 31 October (2400 UT)). The incident SEP spectral fluence
 552 rates and meteorological data are fixed in time in our cal-
 553 culations, which are given by the event-averaged spectral
 554 fluence rates and atmospheric depth-altitude data shown
 555 in Figures 2 and 4, respectively. On the other hand, we
 556 allow the cutoff rigidity to vary in time along the flight
 557 trajectories, according to the magnetospheric magnetic
 558 field response to the real-time solar wind and IMF condi-
 559 tions [Kress et al., 2009]. The physics-based HZETRN code
 560 is used to transport the incident SEP ions through the
 561 atmosphere and calculate the dosimetric quantities. A
 562 unique feature of NAIRAS is the computational efficiency
 563 of the deterministic HZETRN code and the ability to predict
 564 global atmospheric radiation exposure from a physics-based
 565 transport code. Moreover, the geomagnetic effects have
 566 not been quantified sufficiently in the past, and we find
 567 they have a profound effect on SEP atmospheric radiation
 568 exposure. In a future report, we will allow the SEP spectral
 569 fluence rates, cutoff rigidity, and atmospheric depth alti-
 570 tude to all vary according to the real-time data input.

571 4.1. Global SEP Dose Distribution

572 [30] Global SEP atmospheric ionizing radiation exposure
 573 are obtained from a precomputed database. The effective
 574 dose rates are calculated on a fixed 2-D grid in atmospheric
 575 depth and cutoff rigidity. The atmospheric depth grid
 576 extends from zero to 1300 g cm^{-2} , and the cutoff rigidity
 577 grid extends from zero to 19 GV. Both grids have non-
 578 uniform spacing with the highest number of grid points
 579 weighted toward low cutoff rigidities and tropospheric
 580 atmospheric depths. The real-time cutoff rigidities are
 581 computed on the same 2.5×2.5 horizontal grid as the
 582 NCEP/NCAR meteorological data. The precomputed effec-
 583 tive dose rates are interpolated to the real-time cutoff
 584 rigidity and atmospheric depth specified at each hori-
 585 zontal grid point.

586 [31] Figure 5 shows global snapshots of atmospheric
 587 effective dose rates over the Northern Hemisphere polar
 588 region for the Halloween 2003 SEP event 3. The effective
 589 dose rates are shown at three altitudes and for three dif-
 590 ferent magnetic field models used in the cutoff rigidity
 591 simulations. Figure 5 (left) shows exposure rates using the
 592 IGRF field. Figure 5 (middle) shows exposure rates com-
 593 puted for a geomagnetically quiet time prior to the onset
 594 of SEP event 3 using the T05 field (28 October 2003,

0002 UT). Figure 5 (right) shows the exposure rates 595
 using the T05 field at the peak of the geomagnetic 596
 storm (29 October 2003, 2100 UT) during SEP event 3. A 597
 typical cruising altitude for a commercial high-latitude 598
 flight is 11 km. Overlaid on the 11 km effective dose rate 599
 altitude surface are great circle routes for three represen- 600
 tative high-latitude commercial flights: London, England 601
 (LHR) to New York, New York (JFK) (5.75 h flight time); 602
 Chicago, Illinois (ORD) to Stockholm, Sweden (ARN) 603
 (8.42 h flight time), and a combination of two great circle 604
 routes from Chicago, Illinois (ORD) to Beijing, China (PEK) 605
 (13.5 h flight time). 606

[32] There are a number of striking features to be noted 607
 from Figure 5. First, the representation of the geomagnetic 608
 field has a significant influence on SEP atmospheric ion- 609
 izing radiation exposure. Comparing Figure 5 (left) and 610
 Figure 5 (middle) shows that even during geomagnetically 611
 quiet periods, the magnetospheric magnetic field weakens 612
 the overall geomagnetic field with a concomitant increase 613
 in radiation levels. This is seen as a broadening of the 614
 open-closed magnetospheric boundary in the T05 quiet 615
 field compared to the IGRF field. The cutoffs are zero in 616
 the region of open geomagnetic field lines. Thus, effective 617
 dose rates based on the IGRF field are underestimated 618
 even for magnetically quiet times. During strong geo- 619
 magnetic storms, as shown in Figure 5 (right), the area of 620
 open field lines are broadened further, bringing large 621
 exposure rates to much lower latitudes. Effective dose 622
 rates predicted using the IGRF model during a large 623
 geomagnetic storm can be significantly underestimated. 624
 The expansion of the polar region high exposure rates to 625
 lower latitudes, due to geomagnetic effects, is quantified 626
 by calculating hemispheric average effective dose rates 627
 from 40N to the pole. This is denoted by “avg” in Figure 5. 628
 At 11 km, there is roughly an 8% increase in the global 629
 average effective dose rate using T05 quiet field compared 630
 to IGRF. During the geomagnetic storm, there is an ~30% 631
 increase in the global average effective dose rate using T05 632
 storm field compared to IGRF. 633

[33] A second important feature to note in Figure 5 is the 634
 strong altitude dependence due to atmospheric shielding. 635
 The exposure rates are very low at 5 km, independent of 636
 geomagnetic field model used. At 15 km, the exposure 637
 rates are significantly higher than at 11 km. Figure 5 shows 638
 that the SEP effective dose rates increase (decrease) expo- 639
 nentially with increasing (decreasing) altitude. The SEP 640
 exposure rate altitude dependence is a fortunate feature for 641
 the aviation community, since radiation exposure can be 642
 significantly reduced by descending to lower altitudes. 643
 Private business jets will receive more radiation exposure 644
 than commercial aircraft if mitigation procedures are not 645
 taken, since business jet cruising altitudes are roughly 12– 646
 13 km. The altitude dependence of the SEP exposure rates 647
 is quantified in Figure 5 by showing the maximum effec- 648
 tive dose rate at each altitude, which is the exposure rate 649
 at zero cutoff rigidity (i.e., in the polar region of open 650
 geomagnetic field lines). The maximum is denoted “max” 651
 in Figure 5. The exposure rate increases on average by 652

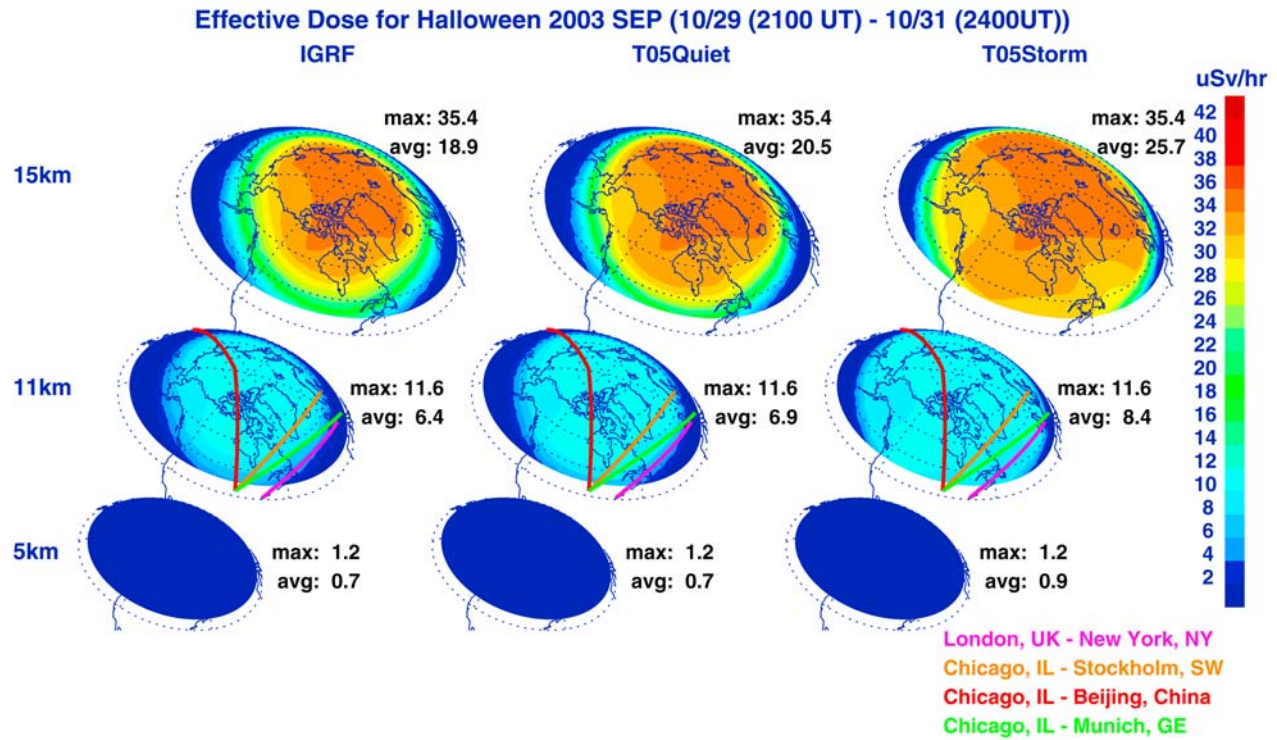


Figure 5. Effective dose rates computed during Halloween 2003 SEP event 3. (left, middle, and right) The plots correspond to exposure rates calculated using the geomagnetic cutoff rigidities and magnetic field models shown in Figure 3. (top, middle, and bottom) Exposure rates calculated at different altitudes. In each image, the hemispheric average dose equivalent rate ($\mu\text{Sv h}^{-1}$) is indicated by the value next to “avg.” The maximum exposure rate is indicated by the value next to “max.” See text for definition of avg and max. Also shown are the magnetic latitude circles and the meridians at 0000, 0600, 1200, and 1800 magnetic local time.

653 $160\% \text{ km}^{-1}$ between 5 km and 11 km. Between 11 km and
 654 15 km, the exposure rate increases on average by approxi-
 655 mately $75\% \text{ km}^{-1}$.

656 [34] It is instructive to compare our results to the
 657 20 January 2005 SEP exposure rates computed by Copeland
 658 *et al.* [2008] using the Monte Carlo MCNPX transport code.
 659 Copeland *et al.* report maximum SEP effective doses of
 660 0.045 mSv and 0.160 mSv at 30 kft (~ 9.1 km) and 40 kft
 661 (~ 12.2 km), respectively, for 1 h continuous exposure at
 662 zero cutoff rigidity. By interpolating these exposure rates
 663 linearly in log dose, we derive a maximum effective dose
 664 rate of $47 \mu\text{Sv h}^{-1}$ at 11 km from the Copeland *et al.* results.
 665 This is a factor of 4 greater than our computed maximum
 666 effective dose rate shown in Figure 5 at 11 km for Halloween
 667 2003 SEP event 3. According to the Copeland *et al.* study,
 668 the January 2005 SEP events produced the largest dose
 669 rates at aviation altitudes during solar cycle 23. On the
 670 other hand, Halloween 2003 SEP event 3 was associated
 671 with one of the five largest geomagnetic storms of solar
 672 cycle 23 [Gopalswamy *et al.*, 2005]. For our purpose of
 673 quantifying the geomagnetic storm effects on SEP exposure
 674 rates, the Halloween 2003 SEP event 3 provides an ideal

storm period for our case study. This is discussed in more
 detail in section 4.2. 675 676

4.2. Dose on High-Latitude Flights 677

[35] Before calculating radiation exposure along speci-
 fied flight paths, it is constructive to examine a sample of
 effective dose rate profiles at different cutoff rigidities
 from our precomputed database previously described for
 SEP event 3. Figure 6 shows SEP effective dose rates as a
 function of atmospheric depth for cutoff rigidities from
 zero to 2.5 GV. Figure 6 clearly shows the exponential
 dependence of SEP exposure on both cutoff rigidity and
 atmospheric depth. The vertical lines indicate constant
 exposure rates necessary to receive a total exposure of 1, 5,
 10, and 20 mSv on an 8 h flight. A typical international,
 high-latitude flight is 8 h. The rationale for choosing the
 total exposure identified with the vertical lines is as fol-
 lows [Wilson *et al.*, 2003]: 20 mSv is the ICRP annual
 occupational radiation worker limit, 10 mSv is the National
 Committee on Radiological Protection (NCRP) annual
 occupational exposure limit, 5 mSv is the NCRP occasional
 public exposure limit, and 1 mSv is the ICRP annual 695

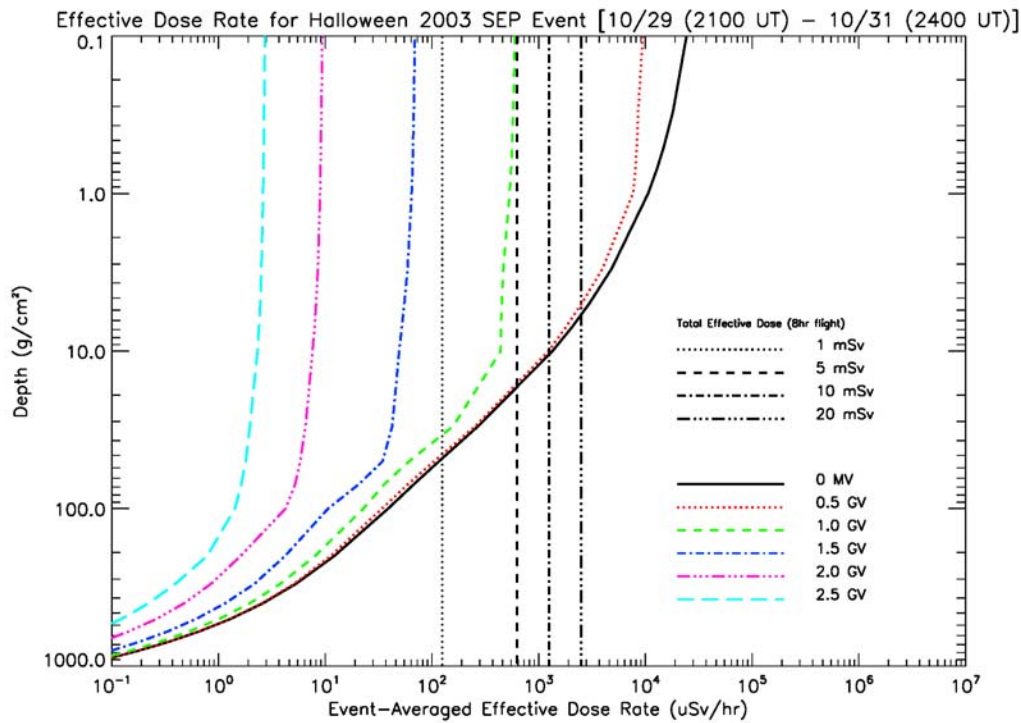


Figure 6. Event-averaged effective dose rates for Halloween SEP event 3 (29 October 2003 (2100 UT) to 31 October 2003 (2400 UT)) as a function of atmospheric depth for various geomagnetic cutoff rigidities. Different vertical lines indicate constant exposure rates required to reach the corresponding total exposure levels indicated in the legend for an 8 h flight.

696 public and prenatal exposure limit. The cutoff rigidities at
 697 high latitudes are less than 1 GV. The typical commercial
 698 airline cruising altitudes correspond to an atmospheric
 699 depth between ~ 200 and 300 g cm^{-2} . Consequently, one
 700 can see from Figure 6 that it is not possible for passengers
 701 on high-latitude commercial flights during the Halloween
 702 2003 SEP events to approach or exceeded the ICRP public
 703 and/or prenatal radiation exposure limit.

704 [36] Figure 7 shows the cutoff rigidities and effective
 705 dose rates for the three representative high-latitude flights
 706 mentioned in section 4.1, which were calculated along
 707 great circle routes. Figure 7 (left) shows the cutoff rigidities
 708 along the flight paths, and Figure 7 (right) shows the
 709 corresponding effective dose rates along the flight paths.
 710 The cutoff rigidities include both latitude and time-
 711 dependent variations along the flight paths. The variations
 712 of the exposure rates along the flight paths include latitu-
 713 dinal variations in both atmospheric depth and cutoff
 714 rigidity. The temporal variations in cutoff rigidity also map
 715 into the variations of the exposure rates along the flight
 716 path. Figure 7 (top) shows results for the LHR-JFK flight,
 717 while Figure 7 (middle and bottom) shows results for the
 718 ORD-ARN and ORD-PEK flights. Each plot in Figure 7
 719 shows cutoff rigidities and corresponding effective dose
 720 rates using the IGRF field (green lines) and the T05 storm

field (red lines) in the cutoff calculations. The largest differ- 721
 722 ences in flight path cutoff rigidities between IGRF and
 723 T05 storm field models are for the LHR-JFK flight. The
 724 entire LHR-JFK flight path is near the magnetosphere
 725 open-closed boundary and is most sensitive to perturba-
 726 tions in cutoff rigidity due to geomagnetic effects. Conse-
 727 quently, the exposure rates along the LHR-JFK flight are
 728 most sensitive to geomagnetic effects. The ORD-PEK polar
 729 route is the least sensitive to geomagnetic suppression of
 730 the cutoff rigidity, since most of the flight path is across the
 731 polar cap region with open geomagnetic field lines. The
 732 influence of geomagnetic storm effects on the ORD-ARN
 733 flight is intermediate between a typical polar route and a
 734 flight along the north Atlantic corridor between the US and
 735 Europe.

736 [37] The effective dose rates for the representative high- 736
 737 latitude flights in Figure 7 are within the range of exposure
 738 rates measured during other storm periods for similar
 739 flight paths. The measurement data were analyzed and
 740 reported in terms of ambient dose equivalent, which is a
 741 reasonable measurement proxy for effective dose. For
 742 example, *Clucas et al.* [2005] reported peak SEP dose rates
 743 in the $3.5\text{--}4.0 \mu\text{Sv h}^{-1}$ range for a LHR-JFK flight on 14 July
 744 2000, a SEP event without a concomitant geomagnetic
 745 storm. From Figure 7, the peak dose rate for the LHR-JFK

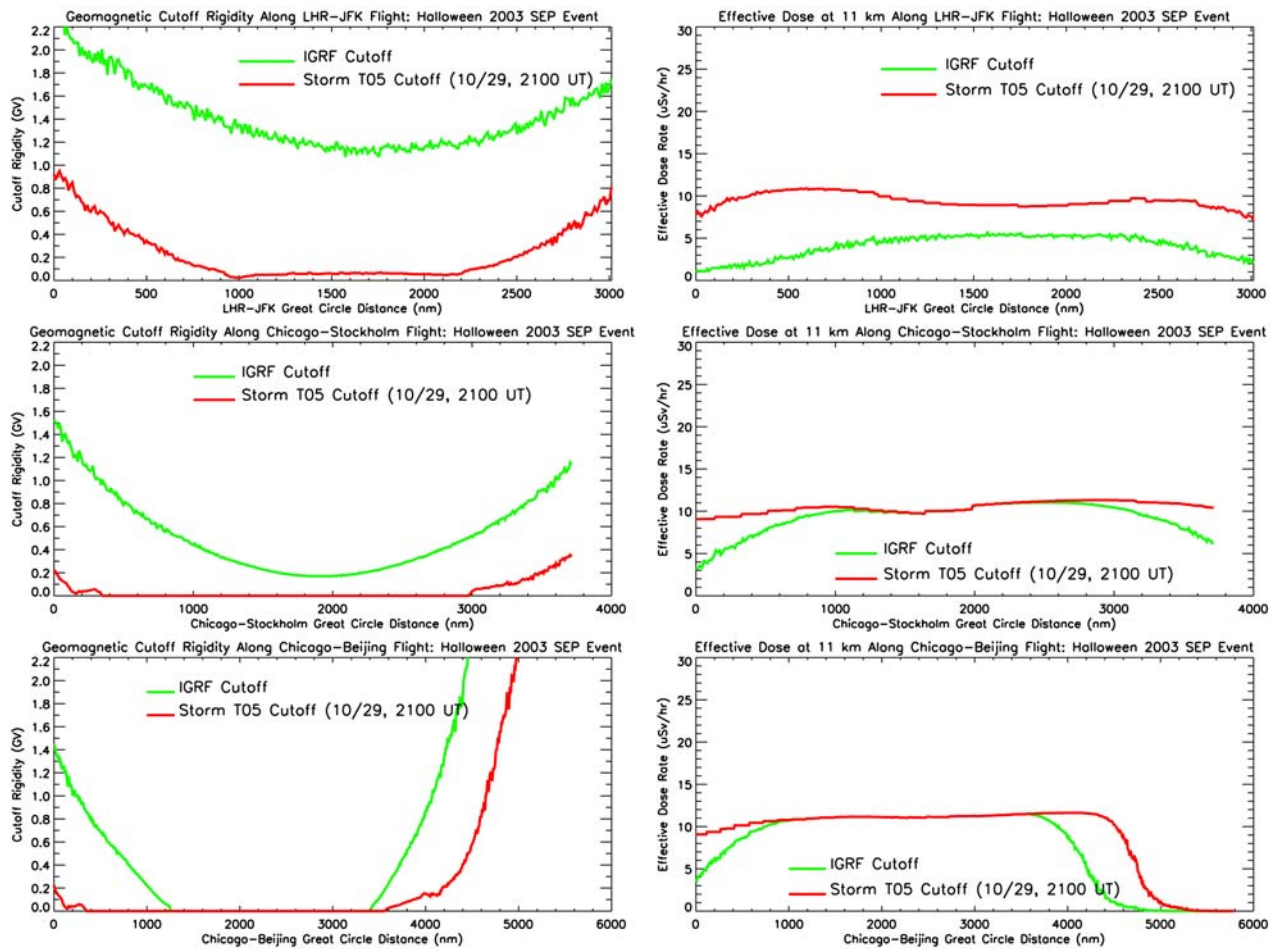


Figure 7. (left) Geomagnetic cutoff rigidities and (right) effective dose rates calculated during Halloween 2003 SEP event 3 along three representative flight paths for a cruising altitude of 11 km. The green line represents cutoff rigidities and exposure rates calculated using the IGRF model. The red lines represent cutoffs and exposure rates computed using the T05 model during the period of largest geomagnetic activity of event 3. The total flight times are the following: 5.75 h for JFK-LHR, 8.42 h for ORD-ARN, and 13.5 h for ORD-PEK.

746 flight computed using the IGRF field is $\sim 4 \mu\text{Sv h}^{-1}$. Clucas
 747 et al. also showed peak measured SEP dose rates on the
 748 order of $10\text{--}12 \mu\text{Sv h}^{-1}$ for a LHR-JFK flight during an
 749 April 2001 SEP event, which was accompanied by a geo-
 750 magnetic storm. The average LHR-JFK effective dose
 751 rate in Figure 7 computed using the T05 storm field is
 752 $9.4 \mu\text{Sv h}^{-1}$. Dyer et al. [2005] reported measured peak
 753 SEP dose rates on the order of $9.5 \mu\text{Sv h}^{-1}$ for a flight
 754 from Prague to New York during the April 2001 SEP
 755 event. Thus, our computed effective dose rates are in
 756 qualitative agreement with measured dose rates for
 757 similar flight paths during other storm periods.

758 [38] The high sensitivity of SEP atmospheric dose rates
 759 to geomagnetic conditions near the open-closed magne-
 760 topheric boundary is also responsible for the high sen-
 761 sitivity of SEP dose rates to the exact flight path in the
 762 north Atlantic corridor region. For example, Dyer et al.

[2007] found that the differences in peak dose rates 763
 between great circle and actual flight paths for LHR-JFK 764
 Concorde flights were a factor of 5 during the September 765
 1989 SEP event and a factor of 2.5 during the October 1989 766
 event, which was geomagnetically quiet. Furthermore, the 767
 difference in peak SEP dose rates between great circle and 768
 actual flight paths for the commercial flight from Prague 769
 to New York during the April 2001 event was a factor of 2. 770

[39] The actual flight paths for the Chicago to Munich 771
 flights reported by Beck et al. [2005] may have been equa- 772
 torward of a great circle route, which could explain their 773
 low dose rates compared to our calculated LHR-JFK great 774
 circle route dose rates during the Halloween 2003 super- 775
 storm. During the Halloween 2003 SEP event 3, the Chicago 776
 to Munich flight measured a mean SEP dose rate of 777
 $3.6 \mu\text{Sv h}^{-1}$ and an accumulated dose of 0.032 mSv for 778
 the 8.75 h flight. These results are comparable to our 779

t2.1 **Table 2.** Flight Path Effective Dose Using Different Geomagnetic Cutoff Models

t2.2 Flight Path	Effective Dose T05 ^a (mSv)	Effective Dose T05Q ^b (mSv)	Effective Dose IGRF ^c (mSv)	Effective Dose Ratio T05S/IGRF	Effective Dose Ratio T05S/T05Q	Effective Dose Ratio T05Q/IGRF
t2.3 JFK-LHR	0.054	0.030	0.024	2.25	1.18	1.25
t2.4 ORD-ARN	0.088	0.084	0.078	1.13	1.05	1.08
t2.5 ORD-PEK	0.122	0.116	0.102	1.20	1.05	1.14

t2.6 ^aCutoff rigidities computed from Tsyganenko (T05) storm fields.t2.7 ^bCutoff rigidities computed from Tsyganenko (T05) quiet time fields.t2.8 ^cCutoff rigidities computed from IGRF fields.

780 5.75 h JFK-LHR for geomagnetically quiet conditions
 781 presented in Figure 7 and Table 2. In other words, the
 782 Chicago to Munich flight did not seem to experience the
 783 dose rate enhancement due to the large geomagnetic storm.
 784 By comparing the LHR-JFK dose rates in Figure 7 computed
 785 using the IGRF field and the T05 storm field with the dose
 786 rates computed for the ORD-ARN and ORD-PEK flights,
 787 it is clear that geomagnetic effects enable flights along
 788 the North Atlantic corridor, or near the magnetosphere
 789 open-closed boundary, to experience the same dose rates
 790 that are confined to the polar region under geomagnetically
 791 quiet conditions.

792 [40] Another possible explanation for the relative dif-
 793 ference in the Chicago to Munich measured dose rates
 794 reported by *Beck et al.* [2005] and our computed dose rates
 795 for the LHR-JFK flight is our use of the event-averaged
 796 incident SEP spectral fluence rate, which we employed for
 797 the purpose of isolating geomagnetic effects in our case
 798 study. It is clear from the shaded regions in Figure 2 that
 799 our event-averaged SEP spectra fluence rate is weighted
 800 more toward the peak ion flux measurements observed
 801 during SEP event 3. The measurements in Figure 1 show
 802 that the SEP ion flux rapidly decreased in time from the
 803 peak values present at the beginning of event 3. Thus, our
 804 use of an event-averaged incident SEP spectral fluence
 805 rate will tend to overestimate the accumulated effective
 806 dose over the flight paths in Figure 7. However, employing
 807 this constraint on the incident SEP spectral fluence rate is
 808 necessary to unambiguously isolate the geomagnetic effects.
 809 Despite these caveats, the results discussed in this paper
 810 are within the current factor of 2 uncertainty in SEP atmo-
 811 spheric dose rates [*Clucas et al.*, 2005].

812 [41] The total effective dose along the three representa-
 813 tive high-latitude flight paths are given in Table 2. The
 814 second, third, and fourth columns show total effective dose
 815 computed from the three models of the geomagnetic field
 816 used in this study: IGRF, T05 quiet field, and T05 storm
 817 field. The last three columns show various ratios between
 818 the total effective dose computed from the different geo-
 819 magnetic field models. There are three major points to be
 820 noted from these results. One, the total effective dose pre-
 821 dicted for the ORD-PEK polar route for SEP event 3 during
 822 the Halloween 2003 storm is ~12% of the ICRP public/
 823 prenatal effective dose limit of 1 mSv. Passengers and
 824 crew on high-latitude flights during the Halloween 2003 SEP
 825 event 3 did not come close to approaching the recommended

ICRP exposure limits. Two, using the IGRF field to compute
 the cutoff rigidity can underestimate the total effective dose
 from ~15% for polar routes to over a factor of 2 for flights
 along the north Atlantic corridor. Third, even for SEP
 events without an accompanying geomagnetic storm, using
 the IGRF field in cutoff rigidity simulations can underesti-
 mate the total effective dose by roughly 20%–30% for US
 flights into Europe.

[42] It is also instructive to compare the total effective
 dose for the ORD-PEK flight in Table 2 with result from
Copeland et al. [2008] during the 20 January 2005 SEP event.
Copeland et al. report maximum SEP effective doses of
 0.088 mSv and 0.320 mSv at 30 kft and 40 kft, respectively,
 for 10 h of continuous exposure at zero cutoff rigidity. This
 corresponds to a total effective dose of 0.123 mSv at 11 km,
 which is nearly equal to the total effective dose for the
 13.5 h ORD-PEK flight in Table 2. The average dose rates
 for the ORD-PEK flight in Table 2 are 9.0 $\mu\text{Sv h}^{-1}$ and
 7.5 $\mu\text{Sv h}^{-1}$ for the T05 storm field and the IGRF field,
 respectively. Using these average dose rates to adjust the
 ORD-PEK total effective dose in Table 2 for a 10 h flight,
 we find the accumulated effective dose to be between
 0.076 mSv and 0.091 mSv, which brings our result to within
 25%–50% of the *Copeland et al.* result. Evidently, our use
 of the event-averaged incident SEP spectral fluence rate
 for the duration of a 10 h polar flight nearly compensates
 for the factor of 4 difference between the peak dose rate for
 the 20 January 2005 SEP event and event-averaged dose
 rate for the Halloween 2003 SEP event 3, as discussed in
 section 4.1.

[43] Another competing phenomena during the Hal-
 loween 2003 superstorm was the occurrence of several
 Forbush decreases [*Gopalswamy et al.*, 2005]. A Forbush
 decrease is a suppression of the GCR exposure due to the
 interaction of the solar wind with the incident GCR
 particles. At latitudes with cutoff rigidities greater than
 1.0–1.2 GV, the SEP dose rates are comparable to or less
 than the GCR dose rates. Thus, at these latitudes, the
 total GCR+SEP dose rate can be less than the quiet time
 dose rates prior to the SEP event during a Forbush decrease.
Getley et al. [2005a, 2005b] observed the apparent influence
 of a Forbush decrease on dosimetry measurements taken
 on Qantas Flight 107 from Los Angeles, California to New
 York, New York on 29 October 2003. These measurements
 are well suited for testing the ability of NAIRAS to model

871 the reduction in the GCR exposure due to Forbush
872 decreases, which we plan to do in the future.

873 5. Summary and Conclusions

874 [44] The NAIRAS model is a physics-based, global, data-
875 driven nowcast of atmospheric ionizing radiation, with
876 radiation exposure rates calculated from the surface to
877 approximately 100 km. At project completion, which is
878 anticipated in mid-2011, NAIRAS will provide real-time
879 predictions of radiation exposure for both background
880 GCR and SEP events. In this paper we have conducted an
881 analysis of atmospheric ionizing radiation exposure asso-
882 ciated with a high-energy SEP event during the Halloween
883 2003 storm period. The main objective of this paper is to
884 diagnose the influence of geomagnetic storm effects on SEP
885 atmospheric radiation exposure. High-latitude flight paths
886 are the routes most susceptible to significant SEP radiation
887 exposure, since the cutoff rigidity rapidly approaches zero
888 near the magnetosphere open-closed boundary.

889 [45] To achieve our objective of diagnosing the geo-
890 magnetic storm effects on SEP radiation exposure, we
891 calculated the atmospheric effective dose rates using event-
892 averaged incident SEP proton and alpha spectral fluence
893 rates and a static atmospheric depth-altitude relation,
894 while the cutoff rigidity was calculated both statically and
895 dynamically. The static cutoff rigidities were simulated
896 using the IGRF field. The dynamic cutoff rigidities were
897 simulated using the T05 field, which was allowed to
898 respond to the real-time solar wind and IMF conditions.
899 The dynamic cutoff rigidities were computed during a
900 geomagnetically quiet period prior to the high-energy
901 SEP event and during the peak of the geomagnetic storm
902 associated with the high-energy SEP event. The key results
903 of this study are the following. One, ignoring solar wind-
904 magnetosphere interactions during a strong geomagnetic
905 storm, in the calculation of cutoff rigidities, can under-
906 estimate the total exposure by approximately 15% to over
907 a factor of 2. Two, even during geomagnetically quiet
908 conditions, ignoring solar wind-magnetosphere interac-
909 tions can underestimate the total exposure for flights
910 along the north Atlantic corridor by roughly 20%–30%.
911 To achieve more accurate assessments of aircraft radiation
912 dose, the magnetospheric influence on the cutoff rigidi-
913 ties must be included routinely in atmospheric radiation
914 exposure predictions.

915 [46] We also showed that the SEP exposure rates increase
916 (decrease) exponentially with increasing (decreasing) alti-
917 tude. Thus, SEP aircraft radiation exposure can be signifi-
918 cantly reduced by descending to lower altitudes. Business
919 jet cruising altitudes are higher than commercial aircraft.
920 Consequently, private jets flying similar high-latitude
921 routes as the commercial airlines will receive substantially
922 more radiation if mitigation procedures are not enacted.
923 NAIRAS real-time radiation exposure rate predictions
924 during SEP events will enable the aviation community to
925 make informed decisions concerning radiation risk evalu-

ation and reduction. The Halloween 2003 SEP events did 926
not pose a radiation health risk, however. 927

[47] In the future, we will assess the reliability and fea- 928
sibility of predicting the real-time geomagnetic cutoff 929
rigidities using the physics-based LFM MHD magnetic 930
fields. The LFM MHD code may be run as a stand alone 931
model or coupled with other geospace models currently 932
under development within CISM. For example, the LFM 933
magnetospheric magnetic fields may be coupled with the 934
Thermosphere-Ionosphere Nested Grid (TING) model 935
[Wang *et al.*, 2004] and/or with the Rice Convection Model 936
(RCM) [Toffoletto *et al.*, 2004], which models the ring current. 937
The semiempirical T05 model provides more accurate 938
cutoff rigidities than the stand alone LFM MHD model, as 939
determined by comparisons with satellite observations 940
during a Halloween 2003 geomagnetic storm [Kress *et al.*, 941
2009]. This is mainly due to the lack of a full kinetic 942
description of the ring current in the MHD model, which 943
typically causes the LFM fields to be too high. We anticipate 944
that the fully coupled LFM-RCM-TING model currently 945
under development will significantly improve the simula- 946
tions of cutoff rigidities compared to the stand along LFM 947
MHD model. Furthermore, the physics-based LFM-RCM- 948
TING model will be able to incorporate short time scale 949
dynamics not included in empirical magnetospheric mag- 950
netic field models. When the code development within 951
CISM reaches sufficient maturity, we will assess the influ- 952
ence of short time scale magnetospheric dynamics on the 953
atmospheric ionizing radiation field using the fully coupled 954
LFM-RCM-TING model. 955

[48] Additionally, our future efforts will build upon this 956
work in six other ways. One, we will study directional 957
effects on the cutoff rigidities and subsequent radiation 958
exposure rates. Two, we will model the aircraft fuselage in 959
calculating radiation exposure. Three, we will allow the 960
SEP spectral fluence rate and atmospheric pressure to 961
vary with time according to the real-time input data. Four, 962
we will analyze additional storm periods to further quantify 963
the relative contributions of SEP spectral fluence rate, 964
geomagnetic activity, and meteorological variability on 965
atmospheric radiation exposure. Five, we will utilize real- 966
time neutron monitor count rates to supplement the 967
satellite ion flux measurements to better constrain the 968
high-energy portion of the incident SEP spectral fluence 969
rates beyond ~ 500 MeV n^{-1} . And six, we will compare 970
our predictions with previous and future onboard aircraft 971
dosimetric measurements. 972

[49] Acknowledgments. This work was supported by the NASA 973
Applied Science Program. C.J.M. is grateful to Xiaojing Xu (SSAI, 974
Inc.) for improving the graphics and for helpful discussions with 975
Barbara Grajewski (National Institute for Occupational Safety and 976
Health). 977

References 978

Aspholm, R., M.-L. Lindbohm, H. Paakkulainen, H. Taskinen, 979
T. Nurminen, and A. Tiitinen (1999), Spontaneous abortions among 980
Finnish flight attendants, *J. Occup. Environ. Med.*, 41(6), 486–491. 981

- 982 Badavi, F. F., J. E. Nealy, G. de Angelis, J. W. Wilson, M. S. Clowdsley,
983 N. J. Luetke, F. A. Cucinotta, M. D. Weyland, and E. J. Semones
984 (2005), Radiation environment and shielding model validation for
985 CEV design, paper 2005-6651 presented at Space 2005, Am. Inst.
986 of Aeronaut. and Astronaut., Long Beach, Calif., 30 Aug. to 1 Sept.
987 Badavi, F. F., J. K. Tramaglina, J. E. Nealy, and J. W. Wilson (2007a),
988 Low Earth orbit radiation environments and shield model valida-
989 tion for ISS, paper 2007-6046 presented at Space 2007 Conference
990 and Exposition, Am. Inst. of Aeronaut. and Astronaut., Long Beach,
991 Calif., 18–20 Sept.
- 992 Badavi, F. F., C. R. Stewart-Sloan, M. A. Xapsos, J. L. Shinn,
993 J. W. Wilson, and A. Hunter (2007b), Description of a generalized
994 analytical model for the micro-dosimeter response, *NASA Tech.*
995 *Rep.*, NASA/TP-2007-214886.
- 996 Battistoni, G., A. Ferrari, M. Pelliccioni, and R. Villari (2005), Evalua-
997 tion of the dose to aircrew members taking into consideration the
998 aircraft structures, *Adv. Space Res.*, 36, 1645–1652.
- 999 Beck, P., M. Latocha, S. Rollet, and G. Stehno (2005), TEPC reference
1000 measurements at aircraft altitudes during a solar storm, *Adv. Space*
1001 *Res.*, 36, 1627–1633.
- 1002 Brandt, S. (1999), *Data Analysis: Statistical and Computational Methods*
1003 *for Scientists and Engineers*, Springer, New York.
- 1004 Clucas, S. N., C. S. Dyer, and F. Lei (2005), The radiation in the atmo-
1005 sphere during major solar particle events, *Adv. Space Res.*, 36, 1657–
1006 1664.
- 1007 Copeland, K., H. H. Sauer, F. E. Duke, and W. Friedberg (2008), Cosmic
1008 radiation exposure on aircraft occupants on simulated high-latitude
1009 flights during solar proton events from 1 January 1986 through
1010 1 January 2008, *Adv. Space Res.*, 42, 1008–1029.
- 1011 Dyer, C., F. Lei, A. Hands, S. Clucas, and B. Jones (2005), Measure-
1012 ments of the atmospheric radiation environment from CREAM
1013 and comparisons with models for quiet time and solar particle
1014 events, *IEEE Trans. Nucl. Sci.*, 52(6), 2326–2331.
- 1015 Dyer, C., F. Lei, A. Hands, and P. Truscott (2007), Solar particle events
1016 in the QinetiQ Atmospheric Radiation Model, *IEEE Trans. Nucl. Sci.*,
1017 54(4), 1071–1075.
- 1018 Ellison, D. C., and R. Ramaty (1985), Shock acceleration of electrons
1019 and ions in solar flares, *Astrophys. J.*, 298, 400–408.
- 1020 Ferrari, A., M. Pelliccioni, and M. Pillon (1997a), Fluence to effective
1021 dose conversion coefficients for neutrons up to 10 TeV, *Radiat. Prot.*
1022 *Dosim.*, 71(3), 165–173.
- 1023 Ferrari, A., M. Pelliccioni, and M. Pillon (1997b), Fluence to effective
1024 dose and effective dose equivalent conversion coefficients for pro-
1025 tons from 5 MeV to 10 TeV, *Radiat. Prot. Dosim.*, 71(2), 85–91.
- 1026 Getley, I. L., M. L. Duldig, D. F. Smart, and M. A. Shea (2005a), Radia-
1027 tion dose along North American transcontinental flight paths during
1028 quiescent and disturbed geomagnetic conditions, *Space Weather*, 3,
1029 S01004, doi:10.1029/2004SW000110.
- 1030 Getley, I. L., M. L. Duldig, D. F. Smart, and M. A. Shea (2005b), The
1031 applicability of model based aircraft radiation dose estimates, *Adv.*
1032 *Space Res.*, 36, 1638–1644.
- 1033 Gold, R. E., S. M. Krimigis, S. E. Hawkins III, D. K. Haggerty, D. A.
1034 Lohr, E. Fiore, T. P. Armstrong, G. Holland, and L. J. Lanzerotti
1035 (1998), Electron, proton, and alpha monitor on the Advanced Com-
1036 position Explorer spacecraft, *Space Sci. Rev.*, 86, 541–562.
- 1037 Gopalswamy, N., S. Yashiro, Y. Liu, G. Michalek, A. Vourlidas, M. L.
1038 Kaiser, and R. A. Howard (2005), Coronal mass ejections and other
1039 extreme characteristics of the 2003 October–November solar erup-
1040 tions, *J. Geophys. Res.*, 110, A09S15, doi:10.1029/2004JA010958.
- 1041 Haggerty, D. K., E. C. Roelof, G. C. Ho, and R. E. Gold (2006), Quan-
1042 titative comparison of ACE/EPAM data from different detector
1043 heads: Implications for NOAA RTSE users, *Adv. Space Res.*, 38,
1044 995–1000.
- 1045 International Commission on Radiological Protection (ICRP) (1991),
1046 *Recommendations of the International Commission on Radiological Pro-*
1047 *tection*, *Ann. ICRP*, 21(1–3).
- 1048 Kalnay, E., et al. (1996), The NCAR/NCEP 40-year reanalysis project,
1049 *Bull. Am. Meteorol. Soc.*, 77, 437–471.
- 1050 Kress, B. T., M. K. Hudson, K. L. Perry, and P. L. Slocum (2004),
1051 Dynamic modeling of geomagnetic cutoff for the 23–24 November
1052 2001 solar energetic particle event, *Geophys. Res. Lett.*, 31, L04808,
1053 doi:10.1029/2003GL018599.
- Kress, B. T., C. J. Mertens, and M. Wiltberger (2009), Solar energetic
1054 particle cutoff variations during the 28–31 October 2003 geomagnetic
1055 storm, submitted to *Space Weather*.
- Langlais, B., and M. Mandea (2000), An IGRF candidate geomagnetic
1057 field model for epoch 2000 and a secular variation model for 2000–
1058 2005, *Earth Planets Space*, 57, 1137–1148.
- Lauria, L., T. J. Ballard, M. Caldora, C. Mazzanti, and A. Verdecchia
1060 (2006), Reproductive disorders and pregnancy outcomes among
1061 female flight attendants, *Aviat. Space Environ. Med.*, 77(7), 533–559,
1062
- Lewis, B. J., G. I. Bennett, A. R. Green, M. J. McCall, B. Ellaschuk,
1063 A. Butler, and M. Pierre (2002), Galactic and solar radiation exposure
1064 to aircrew during a solar cycle, *Radiat. Prot. Dosim.*, 102(3), 207–227,
1065
- Lindborg, L., D. T. Bartlett, P. Beck, I. R. McAulay, K. Schnuer,
1066 H. Schraube, and F. Spurny (Eds.) (2004), *Cosmic Radiation Exposure of*
1067 *Aircraft Crew: Compilation of Measured and Calculated Data—A Report*
1068 *of EURADOS Working Group 5*, Eur. Com., Luxembourg.
- 1069 Lyon, J. G., J. A. Fedder, and C. M. Mobarry (2004), The Lyon-Fedder-
1070 Mobarry (LFM) global MHD magnetospheric simulation code,
1071 *J. Atmos. Sol. Terr. Phys.*, 66(15–16), 1333–1350.
- 1072 McMeekin, R. R. (1990), Radiation exposure of air carrier crew-
1073 members, *Advis. Circ. 120-52*, Fed. Aviat. Admin., Washington, D. C.
- 1074 Mertens, C. J., J. W. Wilson, S. R. Blattnig, B. T. Kress, J. W. Norbury,
1075 M. J. Wiltberger, S. C. Solomon, W. K. Tobiska, and J. J. Murray
1076 (2008), Influence of space weather on aircraft ionizing radiation
1077 exposure, paper 2008-0463 presented at 46th Aerospace Sciences
1078 Meeting and Exhibit, Am. Inst. of Aeronaut. and Astronaut., Reno,
1079 Nev., 7–10 Jan.
- 1080 Mewaldt, R. A., C. M. S. Cohen, A. W. Labrador, R. A. Leske, G. M.
1081 Mason, M. I. Desai, M. D. Looper, J. E. Mazur, R. S. Selesnick,
1082 and D. K. Haggerty (2005), Proton, helium, and electron spectra
1083 during the large solar particle events of October–November 2003,
1084 *J. Geophys. Res.*, 110, A09S18, doi:10.1029/2005JA011038.
- 1085 Nealy, J. E., F. A. Cucinotta, J. W. Wilson, F. F. Badavi, T. P. Dachev,
1086 B. T. Tomov, S. A. Walker, G. De Angelis, S. R. Blattnig, and
1087 W. Atwell (2007), Pre-engineering spaceflight validation of environ-
1088 mental models and the 2005 HZETRN simulations code, *Adv. Space*
1089 *Res.*, 4, 1593–1610.
- 1090 NOAA (2009), Solar Proton Events Affecting the Earth Environment,
1091 <http://www.swpc.noaa.gov/ftpdir/indices/SPE.txt>, Space Weather
1092 Predict. Cent., Boulder, Colo., 21 Sept.
- 1093 O'Brien, K., W. Friedberg, D. F. Smart, and H. H. Sauer (1998), The
1094 atmospheric cosmic- and solar energetic particle radiation environ-
1095 ment at aircraft altitudes, *Adv. Space Res.*, 21, 1739–1748.
- 1096 O'Brien, K., D. F. Smart, M. A. Shea, E. Felsberger, U. Schrewe,
1097 W. Friedberg, and K. Copeland (2003), World-wide radiation dose-
1098 age calculations for air crew members, *Adv. Space Res.*, 31, 835–840.
1099
- 1100 Onsager, T. G., et al. (1996), Operational uses of the GOES energetic
1101 particle detectors, in *GOES-8 and Beyond*, edited by E. R. Washwell,
1102 *Proc. SPIE Int. Soc. Opt. Eng.*, 2812, 281–290.
- 1103 Picone, J. M., A. E. Hedin, D. P. Drob, and A. C. Aikin (2002),
1104 NRLMSIS-00 empirical model of the atmosphere: Statistical compar-
1105 isons and scientific issues, *J. Geophys. Res.*, 107(A12), 1468,
1106 doi:10.1029/2002JA009430.
- 1107 Schraube, H., V. Mares, S. Roesler, and W. Heinrich (1999), Experi-
1108 mental verification and calculation of aviation route doses, *Radiat.*
1109 *Prot. Dosim.*, 86(4), 309–315.
- 1110 Slaba, T. C., G. D. Qualls, M. S. Clowdsley, S. R. Blattnig, L. C. Simonsen,
1111 S. A. Walter, and R. C. Singleterry (2009), Analysis of mass averaged
1112 tissue doses in CAM, CAF, MAX, and FAX, *NASA Tech. Rep.*, NASA/
1113 *TP-2009-215562*.
- 1114 Smart, D. F., and M. A. Shea (1994), Geomagnetic cutoffs: A review
1115 for space dosimetry calculations, *Adv. Space Res.*, 14, 10787–10796.
- 1116 Smart, D. F., and M. A. Shea (2005), A review of geomagnetic cut-
1117 off rigidities for Earth-orbiting spacecraft, *Adv. Space Res.*, 36,
1118 2012–2020.
- 1119 Toffoletto, F. R., S. Sazykin, R. W. Spiro, R. A. Wolf, and J. G. Lyon
1120 (2004), RCM meets LFM: Initial results of one-way coupling, *J. Atmos.*
1121 *Sol. Terr. Phys.*, 66(15–16), 1361–1370.
- 1122 Tsyganenko, N. A., and M. I. Sitnov (2005), Modeling the dynamics
1123 of the inner magnetosphere during strong geomagnetic storms,
1124 *J. Geophys. Res.*, 110, A03208, doi:10.1029/2004JA010798.
- 1125 Tylka, A. J., and M. A. Lee (2006), Spectral and compositional charac-
1126 teristics of gradual and impulsive solar energetic particle events,

- 1127 in *Solar Eruptions and Energetic Particles, Geophys. Monogr. Ser.*,
 1128 vol. 165, edited by N. Gopalswamy, R. Mewaldt, and J. Torsti,
 1129 pp. 263–274, AGU, Washington, D. C.
 1130 Tylka, A. J., C. M. S. Cohen, W. F. Dietrich, M. A. Lee, C. G. MacLennan,
 1131 R. A. Mewaldt, C. K. Ng, and D. V. Reames (2005), Shock geometry,
 1132 seed populations, and the origin of variable elemental composition
 1133 at high energies in large gradual solar particle events, *Astrophys. J.*,
 1134 625, 474–495.
 1135 Wang, W., M. Wiltberger, A. G. Burns, S. C. Solomon, T. L. Killeen,
 1136 N. Maruyama, and J. G. Lyon (2004), Initial results from the coupled
 1137 magnetosphere-ionosphere-thermosphere model: Thermosphere-
 1138 ionosphere responses, *J. Atmos. Sol. Terr. Phys.*, 66(15–16), 1425–1441.
 1139 Waters, M., T. F. Bloom, and B. Grajewski (2000), The NIOSH/FAA
 1140 working women’s health study: Evaluation of the cosmic-radiation
 1141 exposures of flight attendants, *Health Phys.*, 79(5), 553–559.
 1142 Wilson, J. W., L. W. Townsend, W. Schimmerling, G. S. Khandelwal,
 1143 F. Khan, J. E. Nealy, F. A. Cucinotta, L. C. Simonsen, J. L. Shinn, and
 1144 J. W. Norbury (1991), Transport methods and interactions for space
 1145 radiations, *NASA Tech. Rep., NASA-RP-1257*.
 1146 Wilson, J. W., I. W. Joes, D. L. Maiden, and P. Goldhagan (Eds.)
 1147 (2003), *Atmospheric Ionizing Radiation (AIR): Analysis, results,*
 1148 *and lessons learned from the June 1997 ER-2 campaign, NASA Conf.*
 1149 *Publ., NASA/CP-2003-212155*.
 1150 Wilson, J. W., J. Tweed, S. A. Walker, F. A. Cucinotta, R. K. Tripathi,
 1151 S. Blattnig, and C. J. Mertens (2005a), A procedure for benchmarking
 1152 laboratory exposures with 1 A GeV iron ions, *Adv. Space Res.*, 35,
 1153 185–193.
 1154 Wilson, J. W., C. J. Mertens, P. Goldhagan, W. Friedberg,
 1155 G. De Angelis, J. M. Clem, K. Copeland, and H. B. Bidasaria
 (2005b), Atmospheric ionizing radiation and human exposure, *NASA*
Tech. Rep., NASA/TP-2005-213935.
 Wilson, J. W., R. K. Tripathi, C. J. Mertens, S. R. Blattnig,
 M. S. Cloudsley, F. A. Cucinotta, J. Tweed, J. H. Heinbockel,
 S. A. Walker, and J. E. Nealy (2005c), Verification and validation:
 High charge and energy (HZE) transport codes and future develop-
 ment, *NASA Tech. Rep., NASA/TP-2005-213784*.
 Wilson, J. W., et al. (2006), International space station: A testbed for
 experimental and computational dosimetry, *Adv. Space Res.*, 37,
 1656–1663.
-
- S. R. Blattnig and T. S. Slaba, NASA Langley Research
 Center, 2 West Reid St., Mail Stop 188E, Hampton, VA 23681-2199,
 USA. (steve.r.blattnig@nasa.gov; tony.c.slaba@nasa.gov)
 M. Engel, Department of Physics, Hamline University, 1536 Hewitt
 Ave., Mail Stop B1807, Saint Paul, MI 55104-1205, USA. (mengel02@
 hamlineuniversity.edu)
 B. T. Kress, Department of Physics and Astronomy, Dartmouth
 College, HB 6127 Wilder Laboratory, Hanover, NH 03755-3528,
 USA. (bkress@dartmouth.edu)
 C. J. Mertens, NASA Langley Research Center, 21 Langley Blvd.,
 Mail Stop 401B, Hampton, VA 23681-2199, USA. (christopher.j.
 mertens@nasa.gov)
 S. C. Solomon and M. Wiltberger, High Altitude Observatory,
 National Center for Atmospheric Research, 3080 Center Green,
 Boulder, CO 80307, USA. (stans@ucar.edu; wiltbemj@ucar.edu)